



Fabrication and Evaluation of Anticancer Potential of Eugenol Incorporated Chitosan-Silver Nanocomposites: *In Vitro*, *In Vivo*, and *In Silico* Studies

Hamid Saeed Shah¹ · Sumera Zaib² · Muhammad Sarfraz³ · A. Alhadhrami⁴ · Mohamed M. Ibrahim⁴ · Aamir Mushtaq⁵ · Faisal Usman⁶ · Memoona Ishtiaq⁷ · Muhammad Sajjad⁸ · Hafiz Muhammad Mazhar Asjad⁹ · Umar Farooq Gohar¹⁰

Received: 29 April 2023 / Accepted: 26 July 2023 / Published online: 8 August 2023
© The Author(s), under exclusive licence to American Association of Pharmaceutical Scientists 2023

Abstract

The expanding global cancer burden necessitates a comprehensive strategy to promote possible therapeutic interventions. Nanomedicine is a cutting-edge approach for treating cancer with minimal adverse effects. In the present study, chitosan-silver nanoparticles (ChAgNPs) containing Eugenol (EGN) were synthesized and evaluated for their anticancer activity against breast cancer cells (MCF-7). The physical, pharmacological, and molecular docking studies were used to characterize these nanoparticles. EGN had been effectively entrapped into hybrid NPs ($84 \pm 7\%$). The EGN-ChAgNPs had a diameter of 128 ± 14 nm, a PDI of 0.472 ± 0.118 , and a zeta potential of 30.58 ± 6.92 mV. Anticancer activity was measured *in vitro* using an SRB assay, and the findings revealed that EGN-ChAgNPs demonstrated stronger anticancer activity against MCF-7 cells ($IC_{50} = 14.87 \pm 5.34$ $\mu\text{g/ml}$) than pure EGN (30.72 ± 4.91 $\mu\text{g/ml}$). To support initial cytotoxicity findings, advanced procedures such as cell cycle analysis and genotoxicity were performed. Tumor weight reduction and survival rate were determined using different groups of mice. Both survival rates and tumor weight reduction were higher in the EGN-ChAgNPs (12.5 mg/kg) treated group than in the pure EGN treated group. Based on protein–ligand interactions, it might be proposed that eugenol had a favorable interaction with Aurora Kinase A. It was observed that C9 had the highest HYDE score of any sample, measuring at -6.8 kJ/mol. These results, in conjunction with physical and pharmacological evaluations, implies that EGN-ChAgNPs may be a suitable drug delivery method for treating breast cancer in a safe and efficient way.

Keywords cancer · chitosan-silver · eugenol · molecular docking · nanoparticle

✉ Hamid Saeed Shah
hamid.saeed@uvas.edu.pk

¹ Institute of Pharmaceutical Sciences, University of Veterinary and Animal Sciences, Lahore 54000, Pakistan

² Department of Basic and Applied Chemistry, Faculty of Science and Technology, University of Central Punjab, Lahore 54590, Pakistan

³ College of Pharmacy, Al Ain University, Al Ain 64141, United Arab Emirates

⁴ Department of Chemistry, College of Science, Taif University, P.O. Box 11090, Taif 21944, Saudi Arabia

⁵ Department of Pharmaceutical Sciences, Government College University, Lahore, Pakistan

⁶ Department of Pharmaceutics, Faculty of Pharmacy, Bahauddin Zakariya University, Multan 66000, Pakistan

⁷ Leads College of Pharmacy, Lahore LEADS University, Lahore, Pakistan

⁸ College of Pharmacy, University of Sargodha, Sargodha, Pakistan

⁹ Department of Pharmaceutical Sciences, Faculty of Biomedical Sciences and Engineering, Pak-Austria Fachhochschule: Institute of Applied Sciences and Technology, Mang, Khanpur Road, Haripur-KPK, Pakistan

¹⁰ Institute of Industrial Biotechnology, Government College University, Lahore, Pakistan

Introduction

Cancer is the second leading cause of death worldwide, claiming around 9.6 million lives in 2018. Every year, almost 16% of all fatalities worldwide are caused by cancer [1]. The anticipated death toll from cancer in 2020 was 10 million individuals globally [2]. Medicinal plants have been used for centuries as both a foundation of modern medicine and a source of traditional cures. Medications derived from medicinal plants are gaining popularity due to their efficacy, cheap cost, and minimal risk of adverse effects [3].

Clove (*Syzygium aromaticum* L.) is used in conventional medicine for a variety of biological activities [4]. Clove phytochemicals consist of hydrocarbons, monoterpenes, phenolic, and sesquiterpenes. [5]. Eugenol, eugenol acetate, and β -caryophyllene are all found in clove oil [6]. Eugenol (4-allyl-2-methoxyphenol) is one of several active compounds with multiple biological benefits, such as antioxidant, carcinogenic, antibacterial, antifungal, and insecticidal properties [7]. Many studies have shown numerous molecular pathways for eugenol's cancer-curing actions. Eugenol has produced apoptosis, cell cycle arrest, proliferation, migration, angiogenesis, and metastasis in a variety of cancer cell lines [8–11].

Nanotechnology is an emerging field that combines the use of nanoscale biomaterials for a variety of pharmacological benefits [12, 13]. Polysaccharides found in marine seaweeds provide a cheap, sustainable source of tailored medicine delivery systems. Chitosan, an intriguing biopolymer among these polysaccharides, has a distinctive combination of properties, including biocompatibility and biodegradability [14, 15].

Silver nanoparticles are one of the most widely used nanomaterials due to their variety of applications as anti-bacterial, anti-cancer and anti-inflammatory effects [16, 17]. By using microorganisms, plant extracts, and fungi, silver nanoparticles may be synthesized without the need of hazardous chemicals [18–21]. Silver nanoparticles developed through green synthesis have excellent anti-cancer properties [22]. Combining the features indicated above to develop nano-hybrids of silver and chitosan is particularly promising for anti-cancer applications [23, 24].

The aim of this work is to synthesize nanoparticles encasing EGN from chitosan polysaccharide and silver, and to assess their anticancer potential using advanced pharmacological and computational methods.

Materials and Methods

Material

4,6-diamidino-2-phenylindole dihydrochloride (DAPI), acetic acid, annexin-V-FITC staining kit, chitosan, chloroform,

dialysis membrane (10 K), dimethyl sulfoxide (DMSO), dulbeccos modified eagles medium (DMEM), ethanol, ethylenediamine-tetra-acetic acid (EDTA), fetal bovine serum (FBS), formaldehyde, lactose, low melting point agarose (LMPA), lysozyme, phosphate-buffered saline (PBS) tablets (pH 7.4), polyvinyl alcohol (PVA), Pure EGN, silver nitrate (AgNO_3), sodium chloride (NaCl), sodium hydroxide (NaOH), sulforhodamine B (SRB) dye, trichloroacetic acid (TCA), tris-base (pH 10.5), tri-sodium citrate ($\text{Na}_3\text{C}_6\text{H}_5\text{O}_7$), triton X-100, trypsin were acquired from Sigma-Aldrich. These compounds were utilized without additional purification.

Methods

Preparation of Hybrid Nanoparticles

According to earlier investigation [25], silver nitrate (AgNO_3) was reduced using tri-sodium citrate ($\text{Na}_3\text{C}_6\text{H}_5\text{O}_7$) to produce AgNPs. To summarize, a 75 ml of AgNO_3 (0.0015 M) was heated in ultrapure H_2O to 90°C while continuously stirring (SH-3 Hot Plate Magnetic Stirrer Tullytown PA, United States). The AgNO_3 solution was then slowly mixed with 15 ml of tri-sodium citrate (1.5% w/v). A successful AgNPs synthesis was indicated by a color shift from clear to a deep yellow after 20 min of continuous stirring [26]. Eugenol was dissolved in a 0.5:1 ethanol–water combination with Tween 80 (0.75% v/v) and added to 3 ml of Ch (750 mg/ml in 1% acetic acid) with continual stirring. The TPP (1.5 ml, 2.4 mM) was then added in a 2:1 (Ch-EGN:TPP, v/v) ratio to the Ch-EGN mixture and stirred for 3 h. After that, 5 ml of AgNPs in a 2:1 AgNP:Ch (v/v) ratio was added dropwise to the Ch-EGN mixture kept on a magnetic stirrer overnight. The obtained nanoparticles were lyophilized by putting them into a glass vial and freezing them for two hours at -40°C in a single chamber LSCplus Martin Christ™ Germany. The lyophilized powder was refrigerated at 4°C until further studies were conducted.

Physical Characterization of EGN-ChAgNPs

Entrapment Efficiency

The percent entrapment efficiency (EE) was evaluated by slightly modifying the previously reported method [27]. The EGN-ChAgNPs (59.5 mg which is equivalent to 50 mg of EGN) was added in 5 mL of PBS (pH 7.4) and injected into a dialysis membrane before being agitated in 500 mL of PBS (pH 7.4) for 1 h at 37°C on a magnetic stirrer set at 100 rpm. The required volume of sample (5 mL) was removed after specified time interval (0 and 1 h) and centrifuged (Hettich EBA 200S, Hettich, Germany) at 8000 rpm ($6153 \times g$) for 15 min. The centrifuge speed was optimized after testing the sample at various RPM (5000, 8000, and 11,000 RPM).

The pellet did not develop at 5000 RPM, which might be attributed to the dilute disperse system and sluggish RPM. At 8000 RPM, the pellet weight was sufficient for further studies. The obtained free drug concentration was quite high at 11,000 RPM, which might be attributed to nanoparticle breaking. The supernatant was decanted and filtered (Nylon filter membranes pore size 0.45 μm , Sigma Aldrich, USA). Without further dilution, the absorbance of sample was taken at 285 nm using UV–visible spectrophotometer (Shimadzu UV 1900i, Tokyo, Japan).

The percent EE was determined using the following formula;

$$EE (\%) = \frac{\text{Total ENG added} - \text{EGN in supernatant}}{\text{Total EGN added}} \times 100$$

Transmission Electron Microscopy

The morphology of the EGN-ChAgNPs (10 μl) was examined by transmission electron microscopy (TEM; JEM-2100; JEOL; Tokyo, Japan; 200 kV) after being negatively stained with 2% uranyl acetate (w/v), dried for 15–20 min, and then placed onto a carbon-coated copper grid (300 mesh) [28].

Hydrodynamic Diameter and Zeta Potential Estimation

The hydrodynamic diameter was determined by dispersing EGN-ChAgNPs in double-distilled water. The sample's hydrodynamic diameter distribution and zeta potential were quantified using Malvern Zetasizer Nano ZS (Cambridge, UK) [29].

Drug Release Kinetics

Based on the previously described approach, we investigated the EGN release pattern and with the help of kinetic models [30]. Briefly, a 59.5 mg of EGN-ChAgNPs equivalent to 50 mg of EGN was dispersed in 5 mL of PBS (pH 7.4) and added into a dialysis membrane which was subsequently submerged in 500 mL of PBS (pH 7.4) containing 1.2 $\mu\text{g}/\text{mL}$ of lysozyme placed on a magnetic stirrer (75 rpm, 37°C). At specified time interval, the UV–visible spectrophotometer (Shimadzu UV 1900i, Tokyo, Japan) was used to assess EGN release at a particular wavelength (285 nm). Release kinetic models were employed using the DDSolver tool to determine the release mechanism of EGN from ChAgNPs.

Stability Test of Nanoparticles

With slight adjustments, a previously described approach was used for stability experiments [31]. The synthesized

AgNPs were kept in a controlled atmosphere (30°C \pm 2°C and RH 65% \pm 5%) provided by a HPP750 stability chamber (Memmert, GmbH, Bavaria, Germany) for a period of 6 months to study their stability according to ICH (International Council for Harmonization) guidelines. To avoid solvent evaporation, a type II glass container is utilized. The UV–vis method was adopted to evaluate the samples.

Pharmacological Characterization

Sulforhodamine B Assay

The SRB assay was used to determine the extent to which pure EGN and EGN-ChAgNPs inhibited cell proliferation in the MCF-7 cell line [32]. The 1×10^4 cells were spread out across 96-well plates and given 24 h to develop. During a 24-h incubation period, varied quantities of pure EGN and EGN-ChAgNPs were added to separate wells. After incubation, cells were fixed with 40% ice-cold trichloroacetic acid (TCA). Afterwards they were washed in PBS and left out to dry in the air. The cells were stained with SRB dye (0.4% w/v) for 30 min. The cells were then mixed with 100 μL of Tris base (10 mM, pH 10.5). At 565 nm, measurements were taken using an ELISA microplate reader ELx808™ (BioTek equipment, Winooski, Vermont, United States). The IC₅₀ ($\mu\text{g}/\text{mL}$) was calculated using Prism 5.0 (GraphPad Software, San Diego, CA, USA).

Genotoxicity Assessment (Comet Assay)

Comet test was used to determine the double-strand DNA (dsDNA) breakage as a part of genotoxicity evaluation utilizing an established procedure [33, 34]. The MCF-7 cell suspension (2×10^4 cells/well) was treated separately for 18 h with pure EGN and EGN-ChAgNPs. Cells treated with 1% LMPA were cultured and then placed on comet slides. The slides were then immersed in a lysis solution of 1% Triton-X, 100 mM EDTA, 2.5 M NaCl, 10 mM Trizma-X, and 10% DMSO at pH 10. The buffering solution (pH 13, 1 mM EDTA, and 300 mM NaOH) for the time-course study was kept in horizontal electrophoresis chambers with the samples. An alkaline buffer was used to unwind the DNA. After that, the slides were washed with CH₃OH, and they were dried completely. Extracted DNA from the comet was analyzed using CaspLab 1.2.3b2 software.

Flow Cytometry Analysis

MCF-7 cells (1×10^4) were treated for 24 h with pure EGN and EGN-ChAgNPs. The cells were detached with trypsin and EDTA for 5 min at 37°C. To prevent cells from clumping together, the cell culture media was added gradually and cautiously. Cells were recovered in 100 μl of binding buffer

for 15 min after being exposed to 500 μM H_2O_2 . The cells were then treated for 15 min individually with annexin-V FITC fluorescent dye and propidium iodide (PI) before being exposed in an obscure environment.

The cells were examined by fluorescence-activated cell sorting (FACS) with an emission wavelength filter of 600 nm for PI and 545 nm for annexin-V-FITC using FL2-A channel. In one cycle, 10,000 harvested cells were evaluated using the CytoFLEX (Beckman-Coulter Life- Sciences, Brea, California, USA). The results were displayed as a cell cycle analysis graph [35].

Animal Studies

Albino female adult BALB/C mice (Avg. 30 g) were maintained in animal house of Bahauddin Zakariya University Multan (60,800), Pakistan. The mice were retained in a room with a temperature of 25°C, a light/dark cycle of 12 h, with unrefined meal and water available at all times. The stress of overcrowding was reduced for five albino mice by housing them in a steel mesh cage. The animals at Bahauddin Zakariya University in Multan were cared for in compliance with the standards established by the university's ethical committee for the use of animals in scientific research (235/PEC/2022). There were a total of five mice split evenly among four groups. A total of five female mice were each given an injection containing about 4×10^6 MCF-7 cells (100 μL). Over the course of 20 days, the tumor was allowed to grow to a volume of 50–100 mm^3 , which was measured with a digital Vernier caliper (BR1078, China) and the following equation.

$$V(\text{mm}^3) = \frac{1}{2} \times ab^2$$

Where:

V is the estimated tumor volume in cubic units (e.g., mm^3), a is the longest diameter or length of the tumor, and b is the shortest diameter or width of the tumor. Mice groups and their respective treatments are shown in Table I.

The percent tumor inhibition rate (TIR) was used to figure out how well each formulation worked against cancer.

$$\text{TIR}(\%) = \frac{\text{weight of tumor in sample group}}{\text{weight of tumor in control group}} \times 100$$

In Silico Molecular Investigation

Chemical Structure and ADME Analysis

PubChem database of NCBI was used to obtain the structure of EGN and evaluate its chemical and physical parameters. Subsequently, absorption, distribution, metabolism, and

Table I In Both Experimental and Control Groups of Mice, Pure EGN, EGN-ChAgNPs, and Cisplatin were Found to Demonstrate Anticancer Effects

Group	Type of Treatment
1	Without treatment (kept on normal saline)
2	Cancerous mice were given 0.02 mg/kg cisplatin
3	Pure EGN (0.05504 mg/kg) treated cancerous mice
4	EGN-ChAgNPs (0.02676 mg/kg) treated cancerous mice

excretion (ADME) analysis was performed by SwissADME, which not only predicts the pharmacokinetic features of the query compound but also interprets its solubility, medicinal chemistry, and physicochemical properties [36].

Biological Target Prediction and Validation

For *in silico* analysis of EGN anti-cancer activity, it was mandatory to predict the potential target of EGN. Swiss Target Prediction, an online database which contained information of active sites information of more than 3,000 proteins. The software assess the query molecule and predicts likely protein targets on the basis of similarity with known ligands. UniProt Knowledge-base (UniProtKB), validated the selected biological target by authenticating its role in various cancers. Furthermore, protein–protein interactions (PPI) of the target macromolecule were visualized by STRING database [37]. The PPIs were observed by limiting the results to *Homo sapiens* along with a confidence level of < 0.05 .

Molecular Docking

The docking of EGN with the intended protein was carried out using the FlexX feature of SeeSAR version 12.1.0. Aurora A, the intended protein, was obtained from the Protein Data Bank (PDB) with identification no. 5EW9 [38]. Binding site extension was performed in SeeSAR's binding site mode preceding the docking analysis. At least 10 distinct EGN postures were created by varying the target protein's active pocket residues. The construction of these poses is dependent on the incremental construction algorithm. The predicted affinities, torsion angles, clashes, and optimum attributes were analyzed to determine the optimal position.

Ligand Interaction Visualization

The Molecular Visualization Software Discovery Studio 2021 was used in order to investigate the positive interactions that exist between EGN and the amino acid residues that were located in the protein's binding pocket [39]. These beneficial interactions, such as hydrophobic and electrostatic

interactions, as well as others, were indicated by dotted lines of various colors. After that, the hydrogen bond and dehydration energy (HYDE) score of the protein–ligand complex was computed using SeeSAR version 12.1.0 (BioSolveIT GmbH, Sankt Augustin, Germany, 2022).. A better understanding of how each atom of EGN contributes to the projected estimated affinity was gained by visualizing the relative contributions of the favorable and unfavorable atoms [40].

Statistical Analysis

An independent two-sample *t*-test (95%) was used to analyze the cell cycle analysis and genotoxicity assessment. The remaining results of the study were presented as mean and standard deviation (SD). However, Prism 5.0, SPSS 9.0 (SPSS Inc. Chicago, IL, USA), and Microsoft Excel 2010 (Microsoft Corp, Redmond, WA, USA) applications were used.

Results and Discussion

Entrapment Efficacy

According to Table II, the synthesized EGN-ChAgNPs exhibited an excellent entrapment efficiency of around $84 \pm 7\%$. Results demonstrated that EGN was effectively entrapped inside the nanoformulation. Entrapment inside a nanocomposite was dependent on the type and interaction between the therapeutic agent and the nanocomposite itself [41]. Previous research has shown that itraconazole had a greater entrapment efficiency ($94.56 \pm 0.11\%$) inside chitosan embedded silver nanoparticles [42]. Nanocomposites based on chitosan had the potential to preserve the enclosed substance by shielding it from environmental hazards and increasing its solubility in water [43]. In another investigation, the chitosan silver encapsulating ability towards

Calotropis procera extract was tested, and it was shown that nanocarrier displayed a greater percentage of effective encapsulation (%EE), which was around 77.12% [44]. The increased entrapment efficiency found with hybrid nanoparticles is consistent with the data that we uncovered.

One aspect that may improve EGN entrapment efficiency was the ideal amount of Ch used in nanoparticle synthesis. We optimized chitosan amount in formulation by using varying quantities (500, 750, 1000 mg) and tested for entrapment efficiency, zeta potential and hydrodynamic diameter. The optimal concentration was found to be 750 mg that had produced a stable dispersion (> 30), desired hydrodynamic diameter (< 200 nm) and excellent entrapment efficiency ($> 80\%$).

Transmission Electron Microscopy

The evaluation of the surface morphology of EGN-ChAgNPs was carried out by the use of transmission electron microscopy (TEM). Nanoparticles have a spherical form with smooth edges when measured against a scale bar of 200 nm (Fig. 1a). Our findings were in line with those of previous investigations on the surface morphology of ChAgNPs at varying Ag concentrations. It was observed that spherical shaped nanoparticles were generated at low silver concentrations and were homogeneously dispersed in chitosan matrix [45]. A study reported previously demonstrated spherical shape of the hybrid chitosan silver nanoparticles, which validated our suggested EGN-ChAgNPs formulation [28].

Estimation of Hydrodynamic Diameter and Zeta Potential

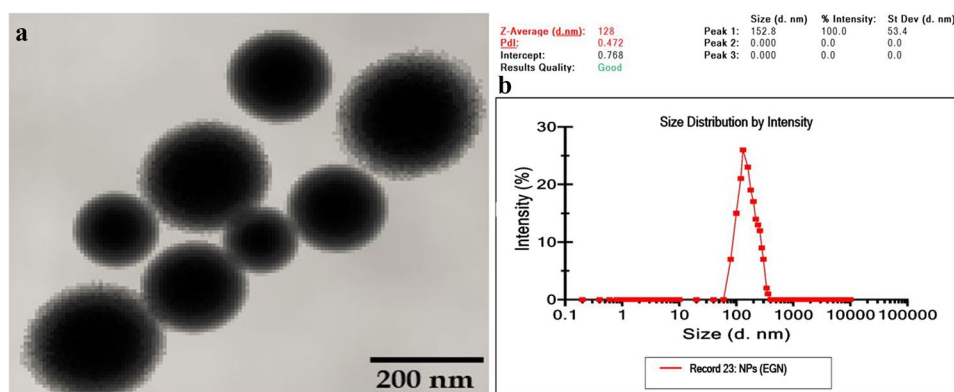
When designing the size of particles, there were two primary considerations that need to be made: the first was that the particles need to be big enough to avoid being eliminated by the kidney [46], and the second was that the particles need to be small enough to avoid being phagocytosed and eliminated by the RES [47]. According to evidence, macromolecules with a molecular weight greater than 40 kDa and nanoparticles with a size range of 10 to 500 nm had the ability to travel through the capillary bed and consolidate in the interstitial region of a tumor to accomplish passive targeting [48]. A study had demonstrated that particles larger than 200 nm were more readily cleared by the body [49].

Figure 1(b) displayed the results of dynamic light scattering (DLS), which was used to establish that hybrid ChAgNPs incorporated EGN indicated the adequate hydrodynamic diameter of approximately 128 ± 14 nm. When it pertains to nanomedicines, the scale of the nanoformulation is of utmost significance because of the importance of its resemblance to bioactive components in order to produce therapeutic effects [50]. The hydrodynamic dimension is a separate measure

Table II Physical Characterization of EGN-ChAgNPs

EGN-ChAgNPs characterization	Findings
Hydrodynamic diameter	128 ± 14 nm
PDI	0.472 ± 0.118
Zero order kinetics	0.9641
First order kinetics	0.9233
Higuchi design	0.8744
Peppas design	0.9780
n-value	0.879
Entrapment efficiency (%)	84 ± 7
Zeta potential	30.58 ± 6.92 mV
IC ₅₀ µg/ml (SRB assay) pure EGN	30.72 ± 4.91
IC ₅₀ µg/ml (SRB assay) EGN-ChAgNPs	14.87 ± 5.34

Fig. 1 Representation of physicochemical characterization of EGN-ChAgNPs, transmission electron microscopy analysis (a) and hydrodynamic diameter of EGN-ChAgNPs (b)



used to determine the stability, dispersion, and biological uptake of nanoparticles in aqueous media [51].

The influence of chitosan on the size of AgNPs was significant due to its terminal glucosamine groups, since it worked as a capping and reducing agent in the synthesis step by transferring electrons to silver ions as an electron acceptor [52]. The current study showed an improvement over a previous study, in which hybrid chitosan silver nanoparticles were found to be 218.4 nm in size [53]. The zeta potential was utilized as a metric to assess the charge, stability, and dispersion potential, thereby verifying the stability of EGN-ChAgNPs. A higher absolute value of the zeta potential signifies greater stability of the system, whereas lower absolute values indicate a tendency of the colloids to agglomerate [54–56].

The zeta potential of the EGN-ChAgNPs was determined to be $+30.58 \pm 6.92$ mV and is presented in Table II. The confirmation of greater dispersion stability was attributed to the higher magnitude of zeta potential. The positive charge on the surface of nanoparticles suggested the existence of repulsive forces that might hinder the aggregation of nanoformulations, thereby preserving their stability. In addition, it was noteworthy that the cell membrane exhibited a slight negative charge, thereby facilitating the electrostatic adsorption of positively charged particles onto the membrane surface by cells [57]. Animal studies had shown that nanoparticles (NPs) with a modest positive charge may concentrate

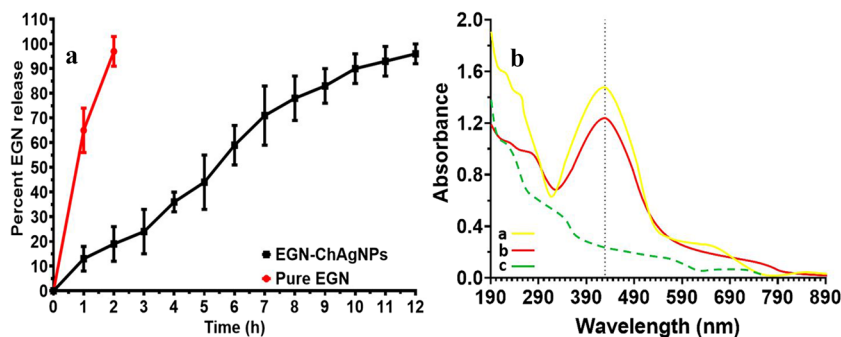
considerably at tumor sites after systemic administration [58].

Drug Release Kinetics

The pure EGN and EGN-ChAgNPs dissolution profile had been seen in Fig. 2(a). Pure EGN was dissolved in medium in 2 h. The kinetic model could not be developed since there were fewer data points owing to rapid dissolution. EGN's short biological half-life, which was believed to be 90 min, may be the cause of its rapid breakdown [59]. However, the release kinetics approach for EGN-ChAgNPs was employed to gain a deeper understanding of the drug releasing mechanism. Various kinetic models were utilized to investigate the nature of the release, including first order, zero order, Korsmeyer-Peppas, and Higuchi models. The R^2 value had served as a metric for evaluating the kinetics and release mechanism of EGN from AgNPs.

Table II had presented an R^2 value of 0.9641 obtained from zero-order analysis, which suggested that drug release was not influenced by concentration at a specific time. It was stated that this kind of kinetic model demonstrated controlled release of a specific substance from hybrid nanoparticles. The Korsmeyer-Peppas model's higher R^2 value (0.9780, $n=0.879$) revealed the swelling and erosion, non-fickian case II type release of EGN from hybrid nanoparticles. In polymeric systems wherein the drug is disseminated or dissolved inside a polymer matrix

Fig. 2 Dissolution profile of EGN-ChAgNPs at 7.4 pH (a), stability analysis of AgNPs when initially synthesized (yellow line), tested for maximum wavelength after six months (red line) and green line (chitosan) appeared with no absorbance peak (b)



or where the drug is chemically bound to the polymer, non-Fickian Case II release is frequently seen. A number of variables, including polymer erosion, expansion and unwinding as well as drug dissolution or diffusion within the polymer matrix, influence the release process [60].

The findings were in agreement with a previous investigation, wherein chitosan nanoparticles exhibited swelling characteristics during the release mechanism of a specific medication. The observed swelling phenomenon could potentially be attributed to the protonation of amino groups, leading to the generation of NH_3^+ . This, in turn, may result in the formation of a gel-like structure through the retention of water [61].

Stability Test of Nanoparticles

The key sign that noble metal nanoparticles have been successfully biosynthesized is a change in the color of the solution from an apparently dull yellow to a yellowish-brown as silver ion (Ag^+) is bio-reduced to metallic AgNPs [62]. The most important method for identifying the formation of metal nanoparticles and demonstrating surface metal plasmon resonance is UV-visible spectroscopy [63].

The UV-visible spectroscopy technique is the most crucial way to determine the creation of metal nanoparticles by revealing the occurrence of metal plasmon resonance at the surface [62]. A prominent signal at 429 nm indicates that the biosynthesized AgNPs have induced surface plasmon resonance (SPR) [63]. Furthermore, the deficiency of any peak in the range of 450 to 800 nm suggests the absence

of agglomeration, which adds to the stability of bioassisted AgNPs [64]. The distinctive absorbance peak that exceeds 400 nm in the UV-vis spectrum is designated as a supporting index for AgNPs generation [26]. Figure 2(b) depicted the UV-vis absorption spectra of the biosynthesized AgNPs following a 6 months storage period to test the AgNPs' stability under ICH guidelines [65].

When compared with the initially created AgNPs solution (Fig. 1b yellow line), no significant shift in the absorption peak or change in the color of the solution was noticed (Fig. 1b red line), suggesting that bioprepared AgNPs had extremely high stability over a long period of time. Our results were corroborated with previously reported studies on stability of biosynthesized AgNPs [31, 65].

Pharmacological Analysis

Sulforhodamine B Assay

The SRB assay was utilized to evaluate the cytotoxicity of both pure EGN and EGN-ChAgNPs on MCF-7 cells Fig. 3(a). MCF-7 cells were exposed to various quantities of pure EGN and EGN-ChAgNPs for a duration of 24 h. The IC_{50} values for pure EGN and EGN-ChAgNPs were estimated to be 30.72 ± 4.91 and 14.87 ± 5.34 $\mu\text{g/ml}$, respectively (Table II).

An earlier investigation reported the anticancer properties of gold (Au) and silver (Ag) nanoparticles conjugated with EGN, on two distinct cancer cell lines, namely HCT116 and MCF-7, across varying concentrations. The EGN-AuNPs

Fig. 3 The pharmacological characterization represents cell death and cell viability percentage of pure EGN and EGN-ChAgNPs nanoparticles (a), Comet assay shows DNA damage in MCF-7 cells treated with pure EGN (b), cisplatin (c), and EGN-ChAgNPs (d)

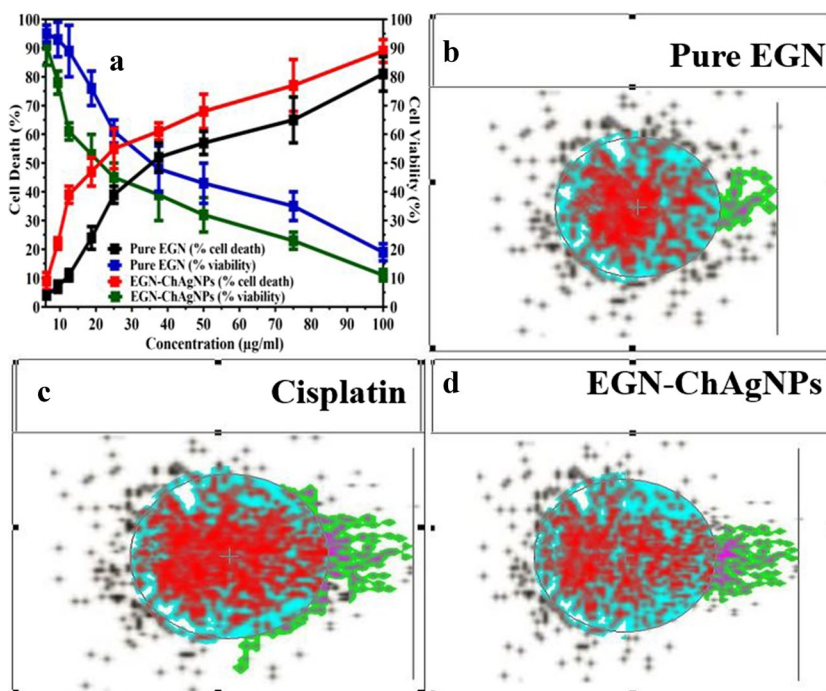


Table III Analysis of Different Parameters of Comet Assay Treated with Cisplatin, EGN-ChAgNPs and Pure EGN on MCF-7 Cell Line

Parameters of comet assay	Cisplatin	EGN-ChAgNPs	Pure EGN
L-Head	195	211	179
L-Tail	88	90	61
L-Comet	283	301	240
Head-DNA	89	90	95
Tail-DNA	10	10	5
TM	09	09	3
OTM	13	11	6

exhibited a significantly higher potency, approximately 18 times greater than that of EGN alone, in inducing cytotoxic effects in both cancer cell lines [66]. Likewise, the encapsulation of EGN in magnetic nanoparticles resulted in the highest inhibition percentage in HeLa cells [67].

Genotoxicity Analysis

DNA damage was verified using the comet test. DNA damage was primarily validated by measuring tail moment (TM), olive tail moment (OTM), and tail DNA as a fraction of total tail DNA. The damaged DNA is transferred to the tail end. The experiment was conducted on MCF-7 cells that were subjected to pure EGN treatment as depicted in Fig. 3(b). Additionally, cisplatin was employed in the assay, as illustrated in Fig. 3(c), along with EGN-ChAgNPs (Fig. 3d). Table III presents the outcomes of various parameters utilized in the comet assay.

The results indicated that EGN-ChAgNPs caused greater DNA damage in MCF-7 cells when compared to pure EGN. The distance travelled by the distorted DNA segments

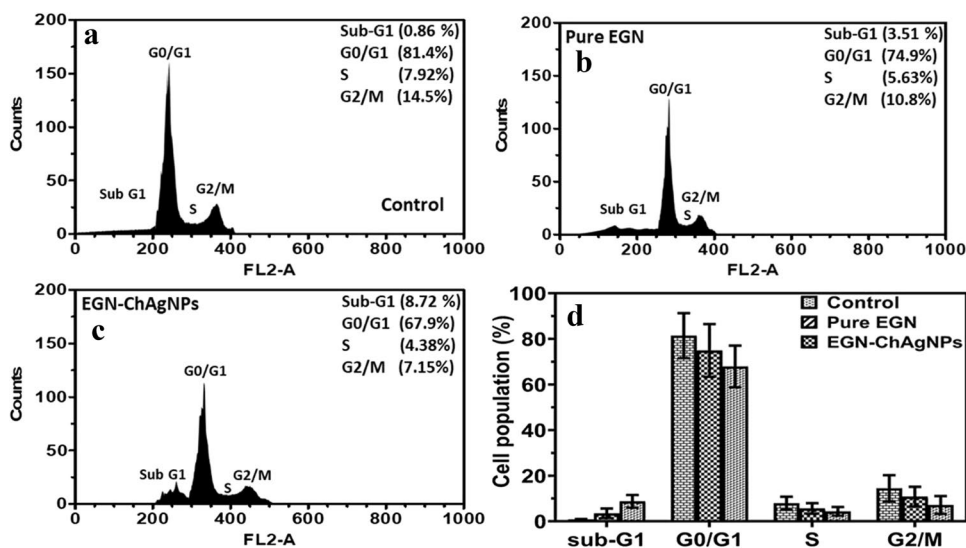
during electrophoresis is represented by a comet tail length (L-Tail). Greater DNA damage is indicated by longer tail lengths, whereas minor or no damage is indicated by shorter tail lengths [68]. Our findings indicated that the L-Tail of EGN-ChAgNPs had a higher numeric value (90) than cisplatin (88), which might be attributed to the bigger L-Head (211) of the comet treated with EGN-ChAgNPs. The Olive tail moment gives a numerical value to the level of DNA damage in a cell. A larger score implies more DNA damage, whereas a lower value indicates less damage [69]. Our research showed that pure EGN had the lowest numerical value of OTM [6], whereas EGN-ChAgNPs had an OTM value that was comparable to cisplatin (11 and 13), respectively.

The comet-like structure formed by DNA fragments migrating out from the nucleus is referred to as the tail movement. The degree of the breakdown of DNA found inside the cells is determined by the amount of tail movement during the comet assay. Less damage results in shorter or missing tails, whereas higher degrees of DNA damage cause greater tail length and intensity. The tail movement in the current investigation revealed similar quantitative information (09) for both cisplatin and EGN-ChAgNPs, whereas it has the lowest value for pure EGN (06), indicating that pure EGN has reduced efficacy. According to previous study, the concentration of damaged DNA tails was reduced in MCF-7 cells treated with Withaferin-A Loaded nanosponges compared to those treated with standard and pure withaferin-A [70].

Flow Cytometry Analysis

Flow cytometry experiment was used to examine the progression of cell arrest data presented in Fig. 4. Earlier techniques provided qualitative confirmation of cancer

Fig. 4 The flow cytometry analysis of control (a), pure EGN (b) and EGN-ChAgNPs (c) treated MCF7 cells. Percentage of cell population in cell cycle treated with control, pure EGN and EGN-ChAgNPs (d)



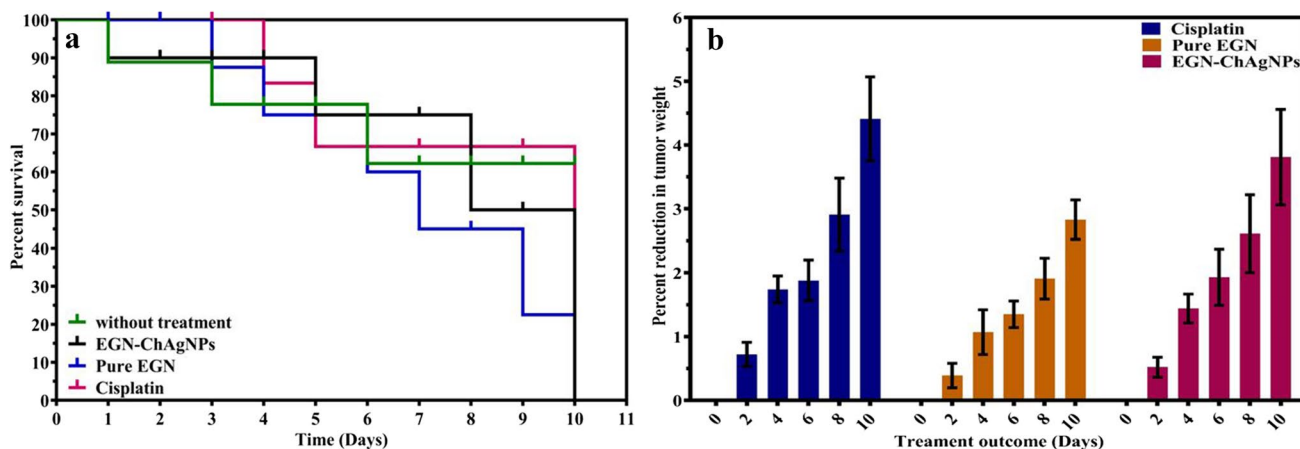


Fig. 5 *In vivo* percent survival rate (a) and percent reduction in tumor weight (b)

cell death; the flow cytometry assay provided quantitative validation of these analysis [71]. Figure 4(a) demonstrates that a higher proportion of MCF-7 cells persisted in the G0/G1 phase following treatment with the control agent. Conversely, when incubated with pure EGN, the cells exhibited a higher rate of mortality, as evidenced by the higher values

of sub-G1 (3.51%) and lower values for G0/G1 (74.9%), as illustrated in the histograms Fig. 4(b). While incubation with EGN-ChAgNPs increased cell mortality, as seen by the greater values of sub-G1 (8.72%) and lower values of G0/G1 (67.9%) in the histograms Fig. 4(c). The findings of our study had aligned with those of a prior investigation, which

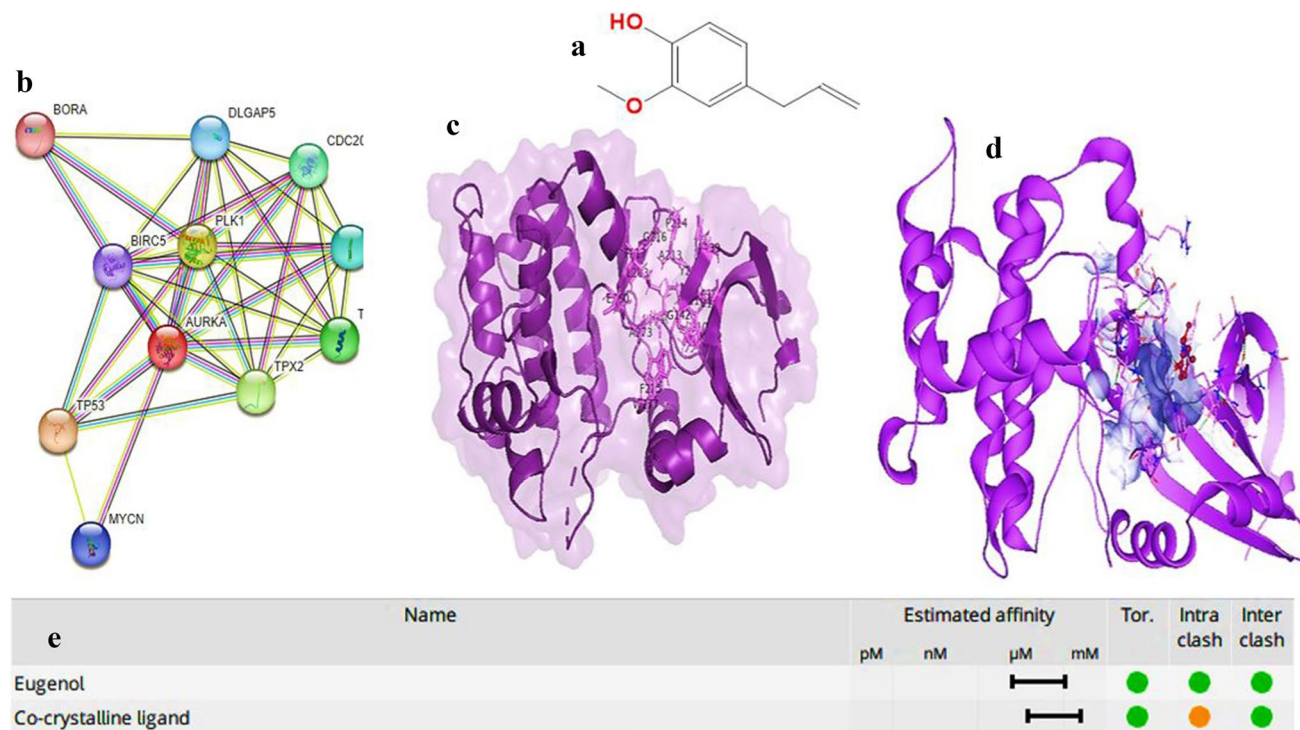


Fig. 6 A 2-dimensional structure of EGN (2-methoxy-4-prop-2-enylphenol) (a), a string network elucidating the protein–protein interaction of Aurora kinase A (AURKA) with other proteins. The color of lines is depicting the type of evidence of interaction between proteins. (light green: textmining; black: co-expression; pink: experimentally determined; light blue: curated databases) (b), representation of active site residues in Aurora kinase A after extending the active

site to 30 residues. These residues include Leu139, Gly140, Gly142, Lys143, Asn146, Val147, Leu159, Ala160, Leu161, Lys162, Leu194, Leu210, Glu211, Tyr212, Ala213, Pro214, Leu215, Gly216, Thr217, Arg220, Lys258, Glu260, Asn261, Leu262, Leu263, Leu264, Ala273, Phe275, Trp277, and Ser278 (c), the docked complex containing the EGN (pink) docked in the active pocket of Aurora Kinase A (purple) (d)

Table IV ADME Analysis of EGN by SwissADME

Attributes	Eugenol
Formula	C ₁₀ H ₁₂ O ₂
Number of heavy atoms	12
Molecular weight (g/mol)	164.20
Fraction Csp ³	0.20
Number of aromatic heavy atoms	6
Number of H-bond acceptors	2
Number of rotatable bonds	3
Number of H-bond donors	1
TPSA (Å ²)	29.46
Molar Refractivity (m ³ mol ⁻¹)	49.06
Class	Soluble
Consensus Log P _{o/w}	2.25
Blood brain barrier	Yes
GI absorption	High
P-gp substrate	No
CYP1A2 inhibitor	Yes
CYP2C9 inhibitor	Yes
CYP2C19 inhibitor	No
CYP3A4 inhibitor	No
CYP2D6 inhibitor	No
Lipinski	Yes; 0 violation
Log K _p (cm/s)	-5.69
PAINS	0 alert
Bioavailability Score	0.55
Synthetic accessibility	1.58

demonstrated that fenugreek protein hydrolysates possess anti-proliferative properties against colorectal cancer cells. Specifically, these hydrolysates were observed to impede cell proliferation by facilitating intrinsic apoptosis [72].

In Vivo Studies

In order to verify the results of the *in vitro* research, an *in vivo* anticancer investigation was carried out using female albino mice. The survival rates of mice given cisplatin (0.02 mg/kg), pure EGN (0.05504 mg/kg), and EGN-ChAgNPs (0.02676 mg/kg) are shown in Fig. 5(a & b). The outcomes were evaluated against the gold standard of cisplatin. Compared to the pure EGN treated group, the EGN-ChAgNPs (0.02676 mg/kg) treated group showed a greater percentage of survivors. In the untreated group, all animals perished within 6 days, but in the EGN and EGN-ChAgNPs groups, the last animal died on days 9 and 10, respectively. These findings were slightly inconsistent with those of Almalki and Naguib (2021), who found that pure EGN dramatically improves survival rates, from 20% in the untreated group to 100% [73].

The group that received EGN-ChAgNPs exhibited a greater reduction in tumor weight percentage on the tenth day following administration, in comparison to the group that received solely pure EGN treatment. The *in vivo* cytotoxicity of pure EGN against tumor cells was augmented through its conversion into hybrid nanoparticles. Prior research had corroborated our present study's findings regarding the advantages of nanoparticles in facilitating controlled and targeted drug delivery, thereby augmenting treatment efficacy across various cancer therapies.

Molecular Docking

Ligand Structure Retrieval and ADME Analysis

The 2D structure of EGN was retrieved from PubChem (PubChem CID: 3314) as shown in Fig. 6(a). According to its physical and chemical properties, EGN is a colorless or pale yellow liquid with pungent taste. In addition, it darkens upon exposure to air, decomposes upon heating to emit irritating fumes and is freely soluble in benzene [74].

The EGN is considered to be a viable target for drug development due to its adherence to the established criteria for druggability. According to these criteria, the TPSA should be greater than 20 Å and less than 130 Å, rotatable bonds should be less than 9, and molecular weight should be from 150 to 500 g/mol. Whereas, the log K_p should be negative to prevent the skin permeation. As the skin permeability of a compound decreases by increase in the negative value of log K_p, which is directly correlated with the size of the compound (molecular size) [75, 76]. Additionally, the value synthetic accessibility should be lower (ranges from 1 to 10) as it is essential for selecting a druggable compound. It predicts the ease to synthesize a compound *in vitro* which will be more difficult when value of synthetic accessibility is higher [77].

The pharmacokinetic properties of EGN by SwissADME predicted that EGN has a molecular weight of 164.20 g/mol, 12 hydrogen bond acceptors, 3 rotatable bonds, 2 hydrogen bond acceptors and 1 hydrogen bond donor. The topological surface area (TPSA), molar refractivity, consensus log P and log K_p was predicted to be 29.46 Å, 49.06 m³ mol⁻¹, 2.25, and -5.69 cm/s. It has high gastrointestinal absorption, no PAIN alerts and is synthetically accessible. Moreover, EGN is non-toxic as shown in Table IV.

Druggable Target Prediction and Validation

The structure of the EGN was used as query to predict the target proteins from SwissADME. Total 32 target proteins were predicted based on the structural similarity of EGN with their reported ligands. Among these, serine/threonine-protein kinase Aurora-A was selected after validating its role

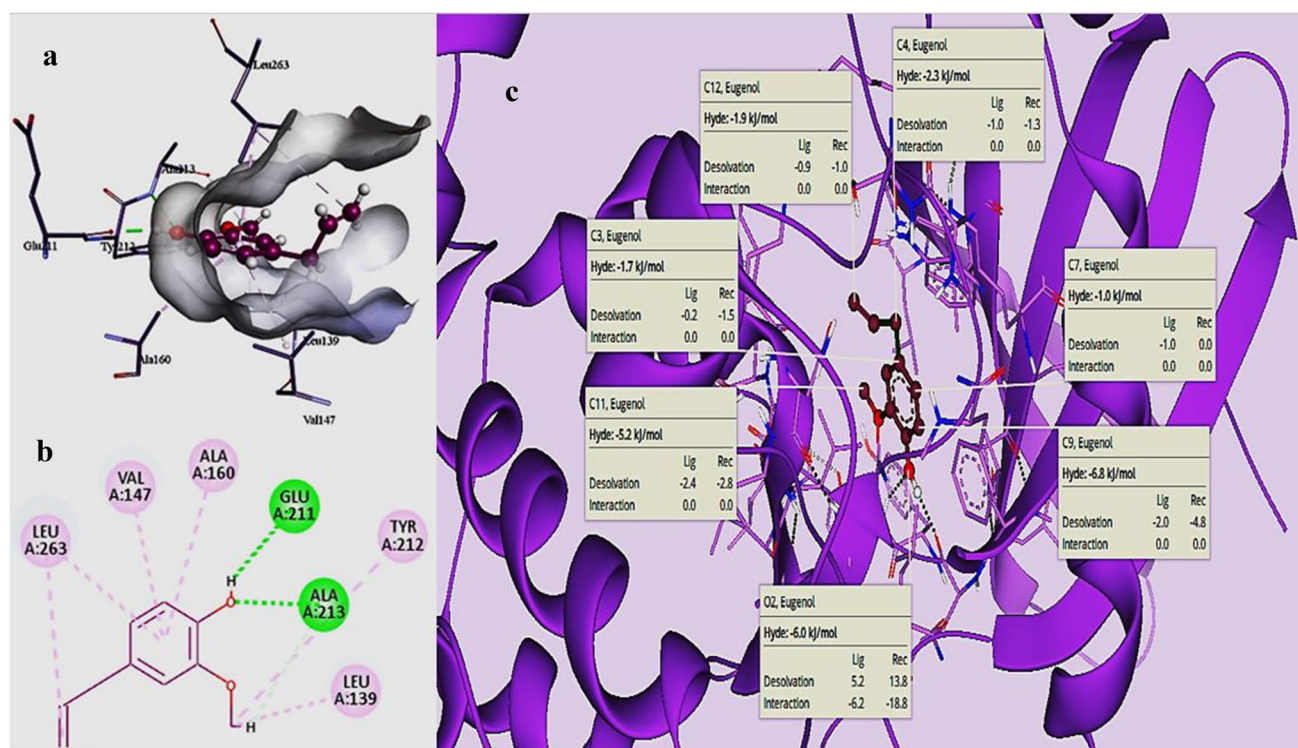


Fig. 7 It is indicating that EGN has greater estimated affinity than the co-crystalline ligand of Aurora Kinase A after standard docking with the FlexX functionality of SeeSAR (a). A 2D representation of protein-ligand interactions, in which the intermolecular interactions are represented by dotted line (Green dotted lines: conventional hydrogen

bond; Pink dotted lines: alkyl and π -alkyl interactions; light blue: carbon hydrogen bond) (b). A 3D representation of protein-ligand interaction of EGN (dark pink) with the active site residues of Aurora kinase A (purple). The HYDE scoring of EGN atoms that have major share in the overall predicted estimated affinity of EGN (c)

in various cancers from UniProtKB (<https://www.uniprot.org/uniprotkb/O14965/entry#expression>). It is specifically upregulated in breast, colon, cervical, ovarian and neuroblastoma cell lines [78]. Owing to this, protein-protein interactions were determined by STRING which predicts that Aurora Kinase A interacts with targeting protein for Xklp2 (TPX2), disks large-associated protein 5 (DLGAP5), protein aurora borealis (BORA), and inner centromere proteins (INCENP). Other proteins include transforming acidic coiled-coil-containing protein 3 (TACC3), polo like kinase 1 (PLK1), cell division cycle protein 20 homolog (CDC20), baculoviral IAP repeat containing 5 (BIRC5), tumor antigen p53 (TP53) and MYCN proto-oncogene (MYCN). Aurora Kinase A interacts with most of the protein by phosphorylating them and regulated the protein that are either involved in cell division or tumor suppression as represented in Fig. 6(b).

Molecular Docking Analysis

Subsequent to validation the 3D structure of Aurora Kinase A was obtained from PDB having a PDB ID of 5EW9. The selected protein has a resolution of 2.18 Å and consists of 271 amino acids with a sole chain (chain A) [79]. The

protein was uploaded in protein mode functionality of SeeSAR in which the protein was extracted with natural ligand to automatically choose the binding site. After standard docking with the co-crystalline ligand in the docking mode, protein-ligand complex was shifted to binding site mode for extending the binding site residues. The most druggable automatically selected binding site had 0.53 DoGSiteScorer, 25 amino acid residues, 0.73 hydrophobicity, 371.52 Å² solvent accessible surface, and 554.90 Å³ volume. The amino acid residues in the binding site were extended from 25 to 30 amino acid residues as shown in Fig. 6(b).

The EGN was then docked to generate poses in the extended binding site of Aurora Kinase A as shown in Fig. 6(c). The results interpreted that Aurora kinase A-EGN complex has greater estimated affinity than the Aurora kinase A-co-crystalline ligand complex. Moreover, the EGN optimally interacts with the binding site of Aurora kinase A with no torsion, intra-clashes observed as elucidated in Fig. 6(d).

Protein-Ligand Interactions

Protein-ligand interactions visualized by Discovery studio predicts that EGN interacts favorably with the Aurora Kinase A via conventional hydrogen bond, carbon hydrogen bond,

alkyl and π -alkyl interactions. The Glu211 and Ala213 of the receptor form the conventional hydrogen bonds with the H22 and O2 of the EGN having a bond length of 1.80 and 2.86 Å, respectively (Fig. 7a). In addition, the carbon hydrogen bond interaction exists between H19 of EGN and oxygen of Ala213 with a bond length of 2.80 Å. A total of 4 π -alkyl interactions are formed between the EGN and receptor binding site. The aromatic ring of EGN develops π -alkyl interactions with three different amino acid residues namely Val147, Ala160 and Leu263. The last π -alkyl intermolecular bond is attributed to the interaction of C11 of the terminal methyl group of EGN with the aromatic ring of Tyr212, which was placed at a distance of 5.34 Å from C11. Moreover, Leu139 and Leu263 interacts with the C11 and C12 of EGN via alkyl bond, respectively as indicated in Fig. 7(b). The HYDE scoring visualized by SeeSAR interprets that C3, C4, C7, C9, C11, C12 and O2 of the EGN have greater contribution in the overall predicted estimated affinity of EGN. The more negative the energy values; the highest will be the HYDE scoring and the atom will be more contributing to the overall affinity. Among these, C9 has the highest HYDE scoring that is -6.8 kJ/mol as shown in Fig. 7(c). It means that among all the atoms of EGN, C9 is significantly responsible for the binding affinity of EGN with aurora kinase A active pocket.

Conclusion

In this work, the hydrodynamic diameter, zeta potential, transmission electron microscopy, electron emission, and release kinetics of EGN-ChAgNPs were measured and characterized. EGN-ChAgNPs were tested for their anticancer effects on MCF-7 cells *in vitro* using SRB, genotoxicity and flow cytometry analysis. Female albino mice were utilized for *in vivo* anticancer tests to corroborate our *in vitro* results. Compared to the pure EGN group, the EGN-ChAgNPs (0.02676 mg/kg) treated group showed a better percentage of survival and tumor weight loss to a greater extent. EGN-ChAgNPs were synthesized in a cost-effective and environmentally friendly manner and shown substantial anticancer activity against breast cancer cells. The HYDE score showed that EGN had contributed more to its predicted affinity. In conclusion, ChAgNPs proved to be a prototype to deliver other naturally occurring medicinal chemicals in cancer therapy.

Acknowledgements The researchers would like to acknowledge Deanship of Scientific Research, Taif University for funding this work.

Author Contributions Conception or design of the work: Hamid Saeed Shah, Faisal Usman and Sumera Zaib Acquisition, analysis, or interpretation of data for the work Hamid Saeed Shah, Faisal Usman, Sumera Zaib, Aamir Mushtaq, Hafiz Muhammad Mazhar Asjad, Muhammad

Sarfraz, Mohamed M. Ibrahim, A. Alhadhrami and Muhammad Sajjad. Drafting the work or revising it critically for important intellectual content: Memoona Ishtiaq and A. Alhadhrami. Final approval of the version to be published: All authors Agreement to be accountable 836 for all aspects of the work in ensuring that questions related to the accuracy or integrity of any part of the work are appropriately investigated and resolved.

Data Availability All the data related to this study are present within the manuscript.

Declarations

Institutional Review Board (IRB) Statement The study design entitled “Fabrication and Evaluation of Anticancer Potential of Eugenol Incorporated Chitosan-Silver Nanocomposites: *in vitro*, *in vivo*, and *in silico* studies” was approved by the research committee on Biosafety and Bioethics (approval number: (235/PEC/22), faculty of pharmacy at Bahauddin Zakariya University Multan (60800), Pakistan. The scientists have been instructed to strictly adhere to guidelines for mice that have previously been authorized by the ethics committee.

Informed Consent Statement Not applicable.

Sample Availability Samples of the compounds are available from the authors on reasonable request.

Conflict of Interest The authors declare no competing interests.

References

1. Wadhwa J, Saigal A. Cancer and COVID-19: Currently in race for the title of “The Emperor of All Maladies!” Indian J Med Paediatr Oncol. 2020;41(03):303–4.
2. Singh D, Vaccarella S, Gini A, De Paula SN, Steliarova-Foucher E, Bray F. Global patterns of Hodgkin lymphoma incidence and mortality in 2020 and a prediction of the future burden in 2040. Int J Cancer. 2022;150(12):1941–7.
3. Zari A, Alfarteesh H, Buckner C, Lafrenie R. Treatment with *Uncaria tomentosa* Promotes Apoptosis in B16-BL6 Mouse Melanoma Cells and Inhibits the Growth of B16-BL6 Tumours. Molecules. 2021;26(4):1066.
4. Mittal M, Gupta N, Parashar P, Mehra V, Khatri M. Phytochemical evaluation and pharmacological activity of *Syzygium aromaticum*: a comprehensive review. Int J Pharm Pharm Sci. 2014;6(8):67–72.
5. El-SaberBatiha G, MagdyBeshbishy A, El-Mleeh A, Abdel-Daim MM, Prasad Devkota H. Traditional uses, bioactive chemical constituents, and pharmacological and toxicological activities of *Glycyrrhiza glabra* L.(Fabaceae). Biomolecules. 2020;10(3):352.
6. Marchese A, Barbieri R, Coppo E, Orhan IE, Daglia M, Nabavi SF, et al. Antimicrobial activity of eugenol and essential oils containing eugenol: A mechanistic viewpoint. Crit Rev Microbiol. 2017;43(6):668–89.
7. Nisar MF, Khadim M, Rafiq M, Chen J, Yang Y, Wan CC. Pharmacological properties and health benefits of eugenol: A comprehensive review. Oxid Med Cell Longevity. 2021;2021:2497354.
8. Abdullah ML, Al-Shabanah O, Hassan ZK, Hafez MM. Eugenol-induced autophagy and apoptosis in breast cancer cells via PI3K/AKT/FOXO3a pathway inhibition. Int J Mol Sci. 2021;22(17):9243.
9. Permatasari HK, Effendi AB, Qhabibi FR, Fawwaz F, Dominique A. Eugenol isolated from *Syzygium aromaticum* inhibits HeLa

- cancer cell migration by altering epithelial-mesenchymal transition protein regulators. *J Appl Pharm Sci.* 2021;11(5):049–53.
10. Petrocelli G, Farabegoli F, Valerii MC, Giovannini C, Sardo A, Spisni E. Molecules present in plant essential oils for prevention and treatment of colorectal cancer (CRC). *Molecules.* 2021;26(4):885.
 11. Yi J-L, Shi S, Shen Y-L, Wang L, Chen H-Y, Zhu J, et al. Myricetin and methyl eugenol combination enhances the anticancer activity, cell cycle arrest and apoptosis induction of cis-platin against HeLa cervical cancer cell lines. *Int J Clin Exp Pathol.* 2015;8(2):1116.
 12. Pautler M, Brenner S. Nanomedicine: promises and challenges for the future of public health. *Int J Nanomed.* 2010;5:803–9.
 13. Tsai N, Lee B, Kim A, Yang R, Pan R, Lee D-K, et al. Nanomedicine for global health. *SLAS Technol.* 2014;19(6):511–6.
 14. Cardozo KH, Guaratini T, Barros MP, Falcão VR, Tonon AP, Lopes NP, et al. Metabolites from algae with economical impact. *Comp Biochem Physiol Part C Toxicol Pharmacol.* 2007;146(1–2):60–78.
 15. Vigneshwaran N, Nachane R, Balasubramanya R, Varadarajan P. A novel one-pot 'green' synthesis of stable silver nanoparticles using soluble starch. *Carbohydr Res.* 2006;341(12):2012–8.
 16. Burduşel A-C, Gherasim O, Grumezescu AM, Mogoantă L, Ficai A, Andronescu E. Biomedical applications of silver nanoparticles: an up-to-date overview. *Nanomater.* 2018;8(9):681.
 17. Faisal N, Kumar K. Polymer and metal nanocomposites in biomedical applications. *Biointerface Res Appl Chem.* 2017;7(6):2286–94.
 18. Yousefzadi M, Rahimi Z, Ghafari V. The green synthesis, characterization and antimicrobial activities of silver nanoparticles synthesized from green alga *Enteromorpha flexuosa* (wulfen). *J Agardh Mater Lett.* 2014;137:1–4.
 19. Kotcherlakota R, Das S, Patra CR. Therapeutic applications of green-synthesized silver nanoparticles. Green synthesis, characterization and applications of nanoparticles. *Micro and Nano Technologies.* 2019;389–428.
 20. Ahmed S, Ahmad M, Swami BL, Ikram S. A review on plants extract mediated synthesis of silver nanoparticles for antimicrobial applications: a green expertise. *J Adv Res.* 2016;7(1):17–28.
 21. Xue B, He D, Gao S, Wang D, Yokoyama K, Wang L. Biosynthesis of silver nanoparticles by the fungus *Arthroderma fulvum* and its antifungal activity against genera of *Candida*, *Aspergillus* and *Fusarium*. *Int J Nanomed.* 2016;11:1899.
 22. Castro-Aceituno V, Ahn S, Simu SY, Singh P, Mathiyalagan R, Lee HA, et al. Anticancer activity of silver nanoparticles from *Panax ginseng* fresh leaves in human cancer cells. *Biomed Pharmacother.* 2016;84:158–65.
 23. Khan Y, Numan M, Ali M, Khali A, Ali T, Abbas N, et al. Bio-synthesized silver nanoparticles using different plant extracts as anti-cancer agent. *J Nanomed Biother Discovery.* 2017;7(154):2.
 24. Sharma H, Mishra PK, Talegaonkar S, Vaidya B. Metal nanoparticles: a theranostic nanotool against cancer. *Drug Discovery Today.* 2015;20(9):1143–51.
 25. Gounden S, Daniels A, Singh M. Chitosan-modified silver nanoparticles enhance cisplatin activity in breast cancer cells. *Biointerface Res Appl Chem.* 2021;11:10572–84.
 26. Varadavenkatesan T, Selvaraj R, Vinayagam R. Green synthesis of silver nanoparticles using *Thunbergia grandiflora* flower extract and its catalytic action in reduction of Congo red dye. *Mater Today Proc.* 2020;23:39–42.
 27. Pushpalatha R, Selvamuthukumar S, Kilimozhi D. Cross-linked, cyclodextrin-based nanosponges for curcumin delivery-Physico-chemical characterization, drug release, stability and cytotoxicity. *J Drug Delivery Sci Technol.* 2018;45:45–53.
 28. Mohamed N. Synthesis of hybrid chitosan silver nanoparticles loaded with doxorubicin with promising anti-cancer activity. *J Bionanosci.* 2020;10(3):758–65.
 29. Varan C, Anceschi A, Sevli S, Bruni N, Giraudo L, Bilgic E, et al. Preparation and characterization of cyclodextrin nanosponges for organic toxic molecule removal. *Int J Pharm.* 2020;585: 119485.
 30. Shah HS, Usman F, Ashfaq-Khan M, Khalil R, Ul-Haq Z, Mushtaq A, et al. Preparation and characterization of anticancer niosomal withaferin-A formulation for improved delivery to cancer cells: *In vitro*, *in vivo*, and *in silico* evaluation. *J Drug Delivery Sci Technol.* 2020;59: 101863.
 31. Rezazadeh NH, Buazar F, Matroodi S. Synergistic effects of combinatorial chitosan and polyphenol biomolecules on enhanced antibacterial activity of biofunctionalized silver nanoparticles. *Sci Rep.* 2020;10(1):19615.
 32. Vichai V, Kirtikara K. Sulforhodamine B colorimetric assay for cytotoxicity screening. *Nat Protoc.* 2006;1(3):1112–6.
 33. Priyadarsini RV, Murugan RS, Maitreyi S, Ramalingam K, Karunakaran D, Nagini S. The flavonoid quercetin induces cell cycle arrest and mitochondria-mediated apoptosis in human cervical cancer (HeLa) cells through p53 induction and NF- κ B inhibition. *Eur J Pharmacol.* 2010;649(1–3):84–91.
 34. Singh NP, McCoy MT, Tice RR, Schneider EL. A simple technique for quantitation of low levels of DNA damage in individual cells. *Exp Cell Res.* 1988;175(1):184–91.
 35. Lin G-J, Jiang G-B, Xie Y-Y, Huang H-L, Liang Z-H, Liu Y-J. Cytotoxicity, apoptosis, cell cycle arrest, reactive oxygen species, mitochondrial membrane potential, and Western blotting analysis of ruthenium (II) complexes. *JBIC J Biol Inorg Chem.* 2013;18:873–82.
 36. Daina A, Michielin O, Zoete V. SwissADME: a free web tool to evaluate pharmacokinetics, drug-likeness and medicinal chemistry friendliness of small molecules. *Sci Rep.* 2017;7(1):42717.
 37. De La Cruz DL, Prokai L, Prokai-Tatrai K. The antagonist pGlu- β Glu-Pro-NH₂ binds to an allosteric site of the thyrotropin-releasing hormone receptor. *Molecules.* 2021;26(17):5397.
 38. Burley SK, Berman HM, Kleywegt GJ, Markley JL, Nakamura H, Velankar S. Protein Data Bank (PDB): the single global macromolecular structure archive. *Methods Mol Biol.* 2017;1607:627–41.
 39. Reulecke I, Lange G, Albrecht J, Klein R, Rarey M. Towards an integrated description of hydrogen bonding and dehydration: decreasing false positives in virtual screening with the HYDE scoring function. *ChemMedChem.* 2008;3(6):885–97.
 40. Schneider N, Lange G, Hindle S, Klein R, Rarey M. A consistent description of HYdrogen bond and DEhydration energies in protein–ligand complexes: methods behind the HYDE scoring function. *J Comput-Aided Mol Des.* 2013;27:15–29.
 41. Liu Q, Duan B, Xu X, Zhang L. Progress in rigid polysaccharide-based nanocomposites with therapeutic functions. *J Mater Chem B.* 2017;5(29):5690–713.
 42. Nguyen N-T, Liu J-H. A green method for *in situ* synthesis of poly (vinyl alcohol)/chitosan hydrogel thin films with entrapped silver nanoparticles. *J Taiwan Inst Chem Eng.* 2014;45(5):2827–33.
 43. Shetta A, Kegere J, Mamdouh W. Comparative study of encapsulated peppermint and green tea essential oils in chitosan nanoparticles: Encapsulation, thermal stability, *in-vitro* release, antioxidant and antibacterial activities. *Int J Biol Macromol.* 2019;126:731–42.
 44. Aftab A, Bashir S, Rafique S, Ghani T, Khan R, Bashir M, et al. Microfluidic platform for encapsulation of plant extract in chitosan microcarriers embedding silver nanoparticles for breast cancer cells. *App Nanosci.* 2020;10:2281–93.
 45. Kumar-Krishnan S, Prokhorov E, Hernández-Iturriaga M, Mota-Morales JD, Vázquez-Lepe M, Kovalenko Y, et al. Chitosan/silver nanocomposites: Synergistic antibacterial action of silver nanoparticles and silver ions. *Eur Polym J.* 2015;67:242–51.
 46. Raj S, Khurana S, Choudhari R, Kesari KK, Kamal MA, Garg N, Ruokolainen J, Das BC, Kumar D. Specific targeting cancer cells with nanoparticles and drug delivery in cancer therapy. *Semin Cancer Biol.* 2021;69:166–77.

47. Betzer O, Shilo M, Opochninsky R, Barnoy E, Motiei M, Okun E, et al. The effect of nanoparticle size on the ability to cross the blood–brain barrier: an *in vivo* study. *Nanomed*. 2017;12(13):1533–46.
48. Torchilin V. Tumor delivery of macromolecular drugs based on the EPR effect. *Adv Drug Delivery Rev*. 2011;63(3):131–5.
49. Parmar K, Patel J, Pathak Y. Factors Affecting the Clearance and Biodistribution of Polymeric Nanoparticles. In: *Pharmacokinetics and Pharmacodynamics of Nanoparticulate Drug Delivery Systems*. Springer; 2022. p. 261–72.
50. Hackley VA, Clogston JD. Measuring the hydrodynamic size of nanoparticles in aqueous media using batch-mode dynamic light scattering. *Methods Mol Bio*. 2011;697:35–52.
51. Chai MHH, Amir N, Yahya N, Saaid IM. Characterization and colloidal stability of surface modified zinc oxide nanoparticle. *J Phys Conf Ser*. IOP Publishing; 2018.
52. Rodriguez-Argueelles MC, Sieiro C, Cao R, Nasi L. Chitosan and silver nanoparticles as pudding with raisins with antimicrobial properties. *J Colloid Interface Sci*. 2011;364(1):80–4.
53. Chen Q, Jiang H, Ye H, Li J, Huang J. Preparation, antibacterial, and antioxidant activities of silver/chitosan composites. *J Carbohydr Chem*. 2014;33(6):298–312.
54. Kurpiers M, Wolf JD, Steinbring C, Zaichik S, Bernkop-Schnürch A. Zeta potential changing nanoemulsions based on phosphate moiety cleavage of a PEGylated surfactant. *J Mol Liq*. 2020;316: 113868.
55. Kamble S, Agrawal S, Cherumukkil S, Sharma V, Jasra RV, Munshi P. Revisiting zeta potential, the key feature of interfacial phenomena, with applications and recent advancements. *ChemistrySelect*. 2022;7(1): e202103084.
56. Larsson M, Hill A, Duffy J. Suspension stability; why particle size, zeta potential and rheology are important. *Annu Trans Nordic Rheol Soc*. 2012;2012(20):6.
57. Albanese A, Tang PS, Chan WC. The effect of nanoparticle size, shape, and surface chemistry on biological systems. *Annu Rev Biomed Eng*. 2012;14:1–16.
58. Zein R, Sharrouf W, Selting K. Physical properties of nanoparticles that result in improved cancer targeting. *J Oncol*. 2020;2020:5194780.
59. Yamazoe Y, Mitsumori K. Assessment of nongenotoxic mechanisms in carcinogenicity test of chemicals; quinone, quinone imine, and quinone methide as examples. *Thresholds of Genotoxic Carcinogens*. 2016;171–92.
60. Qin H, Zhang H, Li L, Zhou X, Li J, Kan C. Preparation and properties of lambda-cyhalothrin/polyurethane drug-loaded nanoemulsions. *RSC Adv*. 2017;7(83):52684–93.
61. Pereira AKdS, Reis DT, Barbosa KM, Scheidt GN, da Costa LS, Santos LSS. Antibacterial effects and ibuprofen release potential using chitosan microspheres loaded with silver nanoparticles. *Carbohydr Res*. 2020;488:107891.
62. Shukl AK, Iravani S. *Green synthesis, characterization and applications of nanoparticles*. Elsevier; 2018.
63. Kahrilas GA, Wally LM, Fredrick SJ, Hiskey M, Prieto AL, Owens JE. Microwave-assisted green synthesis of silver nanoparticles using orange peel extract. *ACS Sustainable Chem Eng*. 2014;2(3):367–76.
64. Gahlawat G, Choudhury AR. A review on the biosynthesis of metal and metal salt nanoparticles by microbes. *RSC Adv*. 2019;9(23):12944–67.
65. Badhwar R, Mangla B, Neupane YR, Khanna K, Popli H. Quercetin loaded silver nanoparticles in hydrogel matrices for diabetic wound healing. *Nanotechnol*. 2021;32(50):505102.
66. Singh AK, Talat M, Singh D, Srivastava O. Biosynthesis of gold and silver nanoparticles by natural precursor clove and their functionalization with amine group. *J Nanopart Res*. 2010;12:1667–75.
67. Shahabadi N, Akbari A, Karampour F, Falsafi M. Cytotoxicity and antibacterial activities of new chemically synthesized magnetic nanoparticles containing eugenol. *J Drug Delivery Sci Technol*. 2019;49:113–22.
68. Clementi E, Garajova Z, Markkanen E. Measuring DNA damage using the alkaline comet assay in cultured cells. *Bio-Protoc*. 2021;11(16):e4119-e.
69. Jagetia GC. Isoquinoline alkaloid berberine exerts its antineoplastic activity by inducing molecular DNA damage in HeLa cells: A comet assay study. *Biol Med*. 2015;7(1):1.
70. Shah HS, Nasrullah U, Zaib S, Usman F, Khan A, Gohar UF, et al. Preparation, characterization, and pharmacological investigation of withaferin-A loaded nanosponges for cancer therapy; *in vitro*, *in vivo* and molecular docking studies. *Molecules*. 2021;26(22):6990.
71. Vijayan S, Divya K, Jisha M. *In vitro* anticancer evaluation of chitosan/biogenic silver nanoparticle conjugate on Si Ha and MDA MB cell lines. *Appl Nanosci*. 2020;10:715–28.
72. Allaoui A, Gascón S, Benomar S, Quero J, Osada J, Nasri M, et al. Protein hydrolysates from fenugreek (*Trigonella foenum graecum*) as nutraceutical molecules in colon cancer treatment. *Nutrients*. 2019;11(4):724.
73. Almalki DA, Naguib DM. Anticancer activity of aqueous fenugreek seed extract against pancreatic cancer, histological evidence. *J Gastrointest Cancer*. 2022;53(3):683–6.
74. Greenstein GR. The Merck index: An encyclopedia of chemicals, drugs, and biologicals. *Ref Rev*. 2007;21(6):40-.
75. Burdock GA. *Fenaroli's handbook of flavor ingredients*. 6th ed. CRC Press; 2016. p. 2159.
76. Burdock GA. *Fenaroli's Handbook of Flavor Ingredients: Volume 2*. CRC Press; 2019.
77. Oliveira FdA, Andrade LN, De Sousa ÉBV, De Sousa DP. Anti-ulcer activity of essential oil constituents. *Molecules*. 2014;19(5):5717–47.
78. Fu J, Bian M, Jiang Q, Zhang C. Roles of Aurora kinases in mitosis and tumorigenesis. *Mol Cancer Res*. 2007;5(1):1–10.
79. De Groot CO, Hsia JE, Anzola JV, Motamedi A, Yoon M, Wong YL, et al. A cell biologist's field guide to aurora kinase inhibitors. *Front Oncol*. 2015;5:285.

Publisher's Note Springer Nature remains neutral with regard to jurisdictional claims in published maps and institutional affiliations.

Springer Nature or its licensor (e.g. a society or other partner) holds exclusive rights to this article under a publishing agreement with the author(s) or other rightsholder(s); author self-archiving of the accepted manuscript version of this article is solely governed by the terms of such publishing agreement and applicable law.